

# Hierarchical structured $\text{ZnFe}_2\text{O}_4@\text{RGO}@\text{TiO}_2$ composite as powerful visible light catalyst for degradation of fulvic acid

Jiantao Feng · Yechen Wang · Yanhui Hou ·  
Liangchao Li

Received: 24 January 2017 / Accepted: 29 March 2017 / Published online: 18 May 2017  
© Springer Science+Business Media Dordrecht 2017

**Abstract** Hierarchical structured  $\text{ZnFe}_2\text{O}_4$ @reduced graphite oxide@ $\text{TiO}_2$  ( $\text{ZnFe}_2\text{O}_4@\text{RGO}@\text{TiO}_2$ ) nanocomposite was prepared by an electrostatic layer-by-layer route, which played a synthetic effect of Fenton oxidation of  $\text{ZnFe}_2\text{O}_4$  and photocatalytic oxidation of  $\text{TiO}_2$  to degrade fulvic acid (FA) solution under visible-light irradiation. In this method, RGO, as the middle layer, can effectively promote the photo-induced electron flow between the  $\text{ZnFe}_2\text{O}_4$  and  $\text{TiO}_2$  and further improve the efficiency of the photo-Fenton oxidation. The influencing factors on photo-Fenton oxidation, including solution pH, catalyst, and  $\text{H}_2\text{O}_2$  dosage, have also been investigated. The results illustrated that the ternary composite presented the enhanced catalytic performance. Under visible light irradiation, the degradation efficiency of the sample on the FA solution can reach 95.4% within 3 h. In addition, the catalyst exhibited superior stability and reusability, and its degradation efficiency was still up to 90% after 5 cycles. Therefore, the composite will be a kind of efficient photocatalyst and had a promising application for visible-light driven destruction of organic pollutants.

**Keywords** Fenton oxidation · Photocatalytic oxidation ·  $\text{ZnFe}_2\text{O}_4$  · RGO ·  $\text{TiO}_2$  · Nanocomposites

## Introduction

Humic substances, served as the plant growth boosters, on the other hand, have become one of sources for the environment pollution. As a typical representative, fulvic acid (FA), a typical natural organic matter with low molecular weight, is widely presented in soils, sediments, and natural water and has become a huge threat to the environment and human health (Yan et al. 2016; Wang et al. 2016). And, it has strong combining ability with heavy metal ions and organic pollutants due to its considerable functional groups, which makes these toxins more difficult to be removed (An et al. 2015; Dong et al. 2016). Furthermore, it is also the main precursor of carcinogenic byproducts generated in the chloride-based disinfection process (Matilainen et al. 2010; Czech 2016). Therefore, the removal of FA appears to be particularly urgent and has resulted in growing interest. To date, many attempts aiming for removing humic substances based on the views from chemical conversion and physical operation have been made, such as biodegradation, photocatalytic degradation, Fenton oxidation, physical adsorption, etc. (Oskoei et al. 2016; Rao et al. 2016; Sehaqui et al. 2016; Trellu et al. 2016). Among of which Fenton oxidation and photocatalytic degradation are considered as the most commonly used, convenient, and powerful routes (Liu et al. 2016; Jung et al. 2013). However, there still exist some limitations for them to achieve satisfying effect in degradation efficiency. For example, during the Fenton oxidation,  $\text{H}_2\text{O}_2$  is activated by  $\text{Fe}^{2+}$  to generate  $\cdot\text{OH}$  (Eq. (1)). However, the recovery of  $\text{Fe}^{2+}$  through Eq. (2)

J. Feng · Y. Wang · Y. Hou · L. Li (✉)  
Key Laboratory of the Ministry of Education for Advanced Catalysis Materials, Department of Chemistry, Zhejiang Normal University, Jinhua 321004, China  
e-mail: sky52@zjnu.cn

is extremely slow (Minella et al. 2014), which needs additional methods employed to Fenton system, such as ultraviolet (UV) light and electrochemical technology (Flores et al. 2016; Giannakis et al. 2016). Furthermore, the high degradation efficiency of Fenton oxidation is always limited to the narrow acidic pH range (pH = 2~4), and a large number of sludge can be produced in the process of Fenton oxidation. As for photocatalytic degradation, it is well known that the inefficient utilization of solar energy and difficult recycle of photocatalytic reagents have been proved to be still a global problem in the process of photocatalytic degradation. So, it is necessary to find an appropriate way to solve these.



ZnFe<sub>2</sub>O<sub>4</sub> (ZF), an inexpensive material with high magnetic behavior and narrow band gap (1.9 eV), has drawn considerable attentions in photocatalytic treatment of contaminants (Feng et al. 2016; Wu et al. 2016; Yang et al. 2015). But, the easy recombination of photo-induced electron-holes has limited its application. However, it is reported that ZF can react with H<sub>2</sub>O<sub>2</sub> to produce  $\bullet OH$  due to its intrinsic peroxidase-like activity (Su et al. 2012), which will show better performance under visible-light/H<sub>2</sub>O<sub>2</sub> process and be applied as Fenton oxidation. Cai et al. (2016) studied the visible light-assisted heterogeneous Fenton with ZnFe<sub>2</sub>O<sub>4</sub> for the degradation of Orange II. It was found that the ZF catalyst exhibited good activity, and stability under visible irradiation and the decolorization efficiency on Orange II was still over 94% after 5 cycles. On the other hand, TiO<sub>2</sub>, a classical semiconductor photocatalyst, has been shown to be superior to other photocatalysts due to its high chemical stability and non-toxicity. But, the application of TiO<sub>2</sub> is still limited by its wide band gap (E<sub>g</sub> = 3.2 eV), weak absorption capability, and high degree of electric-hole recombination. To solve this problem, as reported previously, lots of works have introduced reduced graphene oxide (RGO) to the TiO<sub>2</sub>, which can effectively reduce the band gap of TiO<sub>2</sub>, accelerate the separation of electric-hole, and make full use of visible light to improve the degradation efficiency on contaminants (Liu et al. 2015a, b; Wang et al. 2015a).

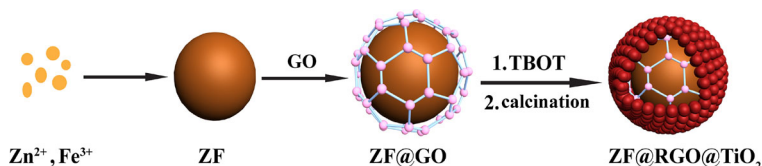
Based on the above assumptions, we herein report first a hierarchical structured ZnFe<sub>2</sub>O<sub>4</sub>@RGO@TiO<sub>2</sub> composite, which plays a synthetic effect of Fenton oxidation of ZF and photocatalytic oxidation of TiO<sub>2</sub> for the degradation of FA. The ZF nanoparticles are encapsulated by GO uniformly, then coated by TiO<sub>2</sub>. After thermal treatment, the anatase TiO<sub>2</sub> shell will be formed and GO will be transferred into RGO in the composite. The advantages of this design can be concluded as follows: First, it is known that when TiO<sub>2</sub> is combined with RGO, the electrons in the valance band of TiO<sub>2</sub> can be excited to conduction band under the irradiation of visible light. Second, as the middle layer, the RGO is not only combined with TiO<sub>2</sub> but also ZF. This special sandwich type makes RGO serve as a conveyor belt, which can transfer quickly the photo-induced electrons arose by ZF and TiO<sub>2</sub> and let them flow between these two components. This will prolong the lifetime of photo-induced electron-hole pairs and promote the reduction of Fe<sup>3+</sup> to Fe<sup>2+</sup>, thus improving the photocatalytic oxidation and Fenton oxidation. Third, the unique coating-coating structure of the composite can extend the contact area of each two components, increasing more active sites of photocatalytic oxidation than ordinary RGO-based composites (Morais et al. 2016; Oliveira et al. 2016; Trapalis et al. 2016). It also should be noted that the RGO possess excellent adsorption capacity, which will further improve the degradation of pollutants. Hence, the core, shell, and the presence of RGO between core and shell can contribute to the degradation of FA, obtaining a better degradation effect. In this work, the influencing factors on degrading FA, including H<sub>2</sub>O<sub>2</sub> dosage, solution pH, and catalyst dosage, have been investigated. In addition, the recyclability and degradation mechanism of ZF@RGO@TiO<sub>2</sub> catalyst have also been discussed thoroughly. And, the schematic illustration of the synthesis of ZF@RGO@TiO<sub>2</sub> is displayed in Fig. 1.

## Experimental section

### Materials

Flake graphite (325 meshes) was obtained from Qingdao Baichuan Graphite Company Ltd. (3-Aminopropyl) trimethoxysilane (APTMS) and tetrabutyl orthotitanate (TBOT) was received from Aladdin Co. Ltd. All other reagents were purchased from Sinopharm Chemical

**Fig. 1** Schematic illustration of the preparation of ZF@RGO@TiO<sub>2</sub>



Reagent Co. Ltd.(China). All reagents were of analytical grade and directly used without any further purification.

#### Preparation of uniform ZnFe<sub>2</sub>O<sub>4</sub> particles

The uniform ZF particles were synthesized according to the method reported previously (Li et al. 2009). Briefly, FeCl<sub>3</sub>·6H<sub>2</sub>O (2.703 g), ZnCl<sub>2</sub> (0.681 g), trisodium citrate (0.8 g), and sodium acetate (NaAc, 7.2 g) were dissolved in ethylene glycol (80 mL) with vigorous stirring. The obtained yellow solution was then transferred into a Teflon-lined stainless-steel autoclaved and heated at 200 °C for 12 h. When cooled, the solid products were washed three times with deionized water and ethanol, followed by drying at 60 °C under vacuum.

#### Synthesis of ZF@GO microspheres

Firstly, GO was prepared via the improved Hummers method (Marcano et al. 2010) from flake graphite and dispersed in deionized water to form suspension for further use. For the encapsulation of GO, 0.2 g ZF was homogeneous dispersed in isopropyl alcohol solution (80 mL) by ultrasonic action for 15 min. Then, APTMS (0.3 mL) were added to the above mixture and refluxed at 80 °C for 24 h. Finally, 20 mL positive ZF suspension was mixed with 50 mL of 1.5 mg/mL negative GO suspension under continuous stirring about 12 h to finish the encapsulation process. ZF@GO microspheres were obtained by drying the separated solid phase to constant weight under vacuum.

#### Synthesis of ZF@GO@TiO<sub>2</sub> composite

The obtained ZF@GO microspheres were further coated by TiO<sub>2</sub> through a kinetics-controlled coating approach (Li et al. 2012). Briefly, 0.2 g of as-prepared ZF@GO microspheres were dispersed in ethanol (100 mL), followed by the addition of NH<sub>3</sub>·H<sub>2</sub>O (0.3 mL). After stirring for 2 min, 0.4 mL of TBOT was added to the above suspension. The mixture was then kept stirring for 24 h at 45 °C. After that, the

resulting products were calcined at 600 °C for 3 h with a ramp rate of 2 °C/min under nitrogen, leading to the formation of ZF@RGO@TiO<sub>2</sub>.

#### Characterization

The X-ray diffraction (XRD) patterns of the samples were obtained by using a Y2000 diffractometer with Cu Kα radiation ( $2\theta = 20^\circ \sim 80^\circ$ ,  $\lambda = 0.15418$  nm,  $0.1$  s<sup>-1</sup>). The morphology, particle size, and element analysis of the synthesized samples were observed by a scanning electron microscopy (SEM, Hitachi S-4800) and a transmission electron microscope (TEM, JEOL2010), respectively. X-ray photoelectron spectroscopy (XPS; PHA-5400, Al Kα radiation) was employed to analyze the chemical composition. The magnetization curve of the product was measured with a vibrating sample magnetometer (LAKE SHORE, 7407). Fourier transform infrared (FT-IR) spectra of samples were recorded on a Nicolet Nexus 670 spectrometer in the range of 400~4000 cm<sup>-1</sup> using KBr pellets. The UV-visible absorption of FA solution was measured with an ultraviolet-visible spectrophotometer (Shimadzu UV-2501PC).

#### Catalytic reaction

The catalytic activity of the as-prepared composite was evaluated by degradation of FA in aqueous solution under visible irradiation ( $\lambda \geq 420$  nm, 300 w). In a typical experiment, 0.1 g of the as-prepared catalyst was added into 50 mL 20 mg/L of FA solution. Before irradiation, the suspension was stirred in the dark for 30 min to reach the adsorption-desorption equilibrium. The light was turned on while a certain amount of H<sub>2</sub>O<sub>2</sub> was added to the mixed solution. The distance between the light source and FA solution is about 45 cm. About 3 mL aliquots were withdrawn at given time intervals, and the catalyst was collected by magnetic separation. The absorbance of suspension determined by spectroscopy at 256 nm was converted to concentration of the remnant FA.

The removal rate of FA ( $Rev$ ) was calculated by the equation

$$Rev = \left(1 - C_t / C_0\right) \times 100\% \quad (3)$$

where  $C_t$  (mg/L) was the concentration of FA at time  $t$ , and  $C_0$  (mg/L) was the initial concentration of FA.

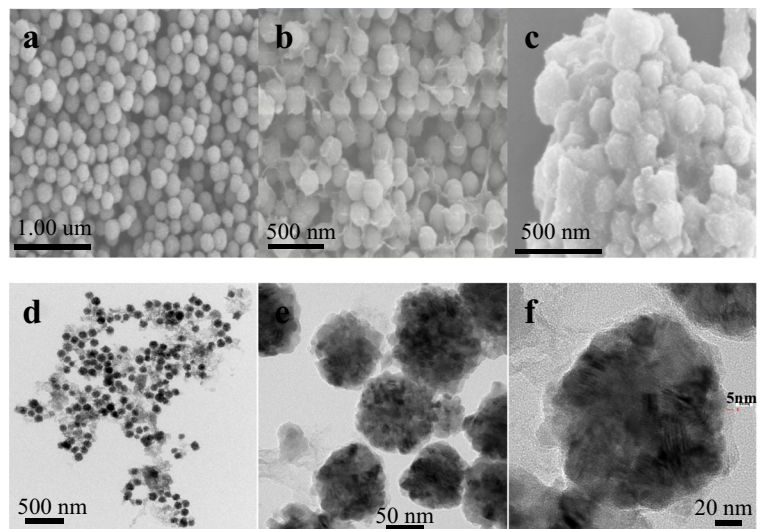
## Results and discussion

### Morphology and structure

The morphology and structure of the samples are displayed in the Fig. 1. And, it can be seen from Fig. 2a that the ZF nanoparticles possess a uniformly spherical shape with a mean diameter of  $150 \pm 20$  nm. After combining with the GO nanosheets, there exist obvious folds on the surface of the ZF nanoparticles (Fig. 2b), which accounts for the successfully integrating GO layers with the ZF particles, and this also corresponds well to the TEM image illustrated in Fig. 2d, which clearly shows that a thin layer is coated on the surface of ZF. The SEM and TEM images presented in Fig. 2c, e explain that the  $TiO_2$  is successfully wrapped on the GO layer. Furthermore, it can be seen that the thickness of the coated  $TiO_2$  layer is about 5 nm from Fig. 2f.

Figure 3 shows the existing elements in the ZF@RGO@ $TiO_2$  composite. As can be seen that the essential elements of Zn, Fe, C, Ti, and O are observed, and their contents are consistent basically with the ratio of stoichiometry in the composite. And, the element of Cu is attributed to the copper net of the sample stage.

**Fig. 2** a SEM images of ZF. b, d SEM and TEM images of ZF@GO. c, e, f SEM and TEM images of ZF@RGO@ $TiO_2$



### XRD analysis

Figure 4 shows the XRD characterization of RGO (a), GO-encapsulated ZF (b), and ZF@RGO@ $TiO_2$  (c). And, it can be seen that the peaks at  $29.9^\circ$ ,  $35.2^\circ$ ,  $42.9^\circ$ ,  $53.2^\circ$ ,  $56.6^\circ$ , and  $62.1^\circ$  correspond to the (220), (311), (400), (422), (511), and (440) crystal face of spinel-structured  $ZnFe_2O_4$  (JCPDS No. 22-1012), respectively. In addition, a wide dispersion peak of GO suggests that the GO nanosheets have amorphous structure in the XRD patterns of ZF@GO (Liu et al. 2015a, b). Two addition peaks located at  $25.2^\circ$  and  $48^\circ$  can be observed after that the  $TiO_2$  nanoparticles are anchored on the surface of ZF@GO and agree with the (101) and (200) crystal face of anatase  $TiO_2$  (Chen et al. 2014). Other characterization peaks of anatase  $TiO_2$ , such as (004), (105), and (204) plane, may be hindered by the crystalline peaks of ZF and cannot be clearly seen in the Fig. 4c.

### FT-IR analysis

FT-IR spectra of the ZF (a), ZF@GO (b), and ZF@RGO@ $TiO_2$  (c) are shown in Fig. 5. The absorption band at  $3433$  and  $1550\text{ cm}^{-1}$  can be regarded as OH groups and the stretching mode of  $H_2O$ , respectively, indicating the existence of absorbed water on the surface of ZF nanoparticles. The peak at  $\sim 2360\text{ cm}^{-1}$  is due to the absorbance of  $CO_2$  from ambient air (Rameshbabu et al. 2014). It also should be noted that the characteristic absorption peaks of the absorbed  $H_2O$  and  $CO_2$  in the composite are stronger than that in the pure ZF (Fig. 5c), illustrating that the as-prepared composites have good

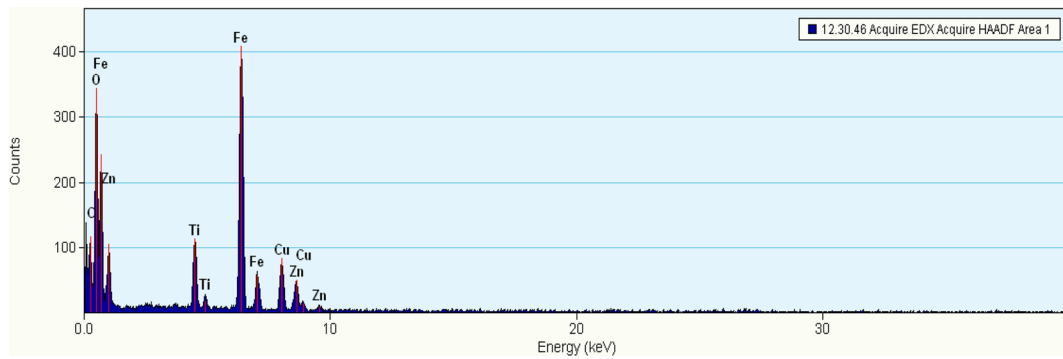


**Fig. 3** EDS analysis of ZF@RGO@TiO<sub>2</sub>

absorption ability. The peaks observed at ~436 and ~556 cm<sup>-1</sup> can be attributed to the tetrahedral Zn<sup>2+</sup> stretching vibration (Zn–O) and the octahedral Fe<sup>3+</sup> stretching vibration (Fe–O), respectively, indicating the presence of ZF (Hou et al. 2013). Additionally, obvious blue shifts of the Fe–O band for the ZF-based composite have been seen after GO doping from Fig. 5b, c. And, a new absorption band situated at ~1627 cm<sup>-1</sup> appears in the FT-IR spectra after being modified by GO, which can be indexed to C=O vibration. Thus, together with the TEM observation, it can be explained by the successful assembling between GO and ZF.

XPS spectra

XPS characterization is performed here to reveal the chemical states of the elements in ZF@RGO@TiO<sub>2</sub> composite, and the corresponding results are presented in Fig. 6. And, it is obvious to be found that the elements of Zn, Fe, O, Ti, and C coexist in the sample. The peaks located at ~1044.0 and ~1021.1 eV are assigned to Zn 2P<sub>1/2</sub> and Zn 2P<sub>3/2</sub>, respectively, indicating the Zn (II)

oxidation state in the ZF. The binding energy peaks for Fe 2P<sub>3/2</sub> at ~712.8 and ~710.9 eV correspond well with the tetrahedral site and octahedral site, respectively, while other peaks at ~725.0 and ~718.9 eV are attributed to the Fe 2p<sub>1/2</sub> and the shakeup satellite structure, respectively. All of the above analyses confirm the existence of ZF in the composite, which is basically identical with the reported literature (Hou et al. 2015; Zhou et al. 2015). As shown in the Fig. 6d, the spin orbit components (2P<sub>1/2</sub> and 2P<sub>3/2</sub>) of Ti 2P peaks located at ~464.2 and ~458.2 eV can be attributed to Ti<sup>4+</sup> in the TiO<sub>2</sub> lattice (Hidalgo et al. 2011). Additionally, compared to the C 1s peaks deconvoluted before reduction (Fig. 6e), the ZF@RGO@TiO<sub>2</sub> composite exhibits a higher ratio of non-oxygenated C to the carbonyl C (Fig. 6d), indicating a considerable reduction for the GO nanosheets. Besides, an additional shoulder peak located at ~288.6 eV is found, which is usually assigned to the formation of C–Ti band (Wu et al. 2009), suggesting that the TiO<sub>2</sub> nanoparticles have been successfully coated on the surface of GO.

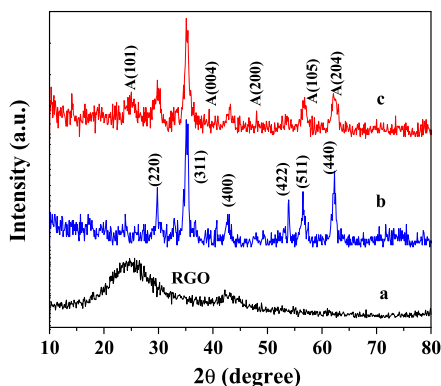


**Fig. 4** XRD patterns of RGO (a), ZF@GO (b), and ZF@RGO@TiO<sub>2</sub> (c)

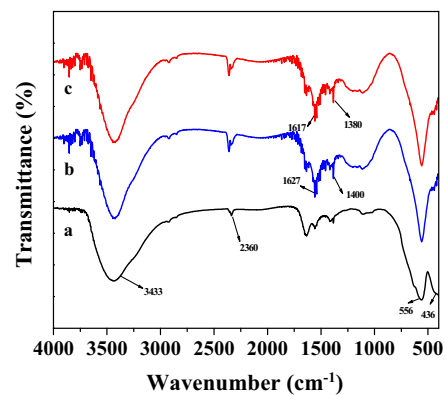


**Fig. 5** FT-IR patterns of ZF (a), ZF@GO (b), and ZF@RGO@TiO<sub>2</sub> (c)



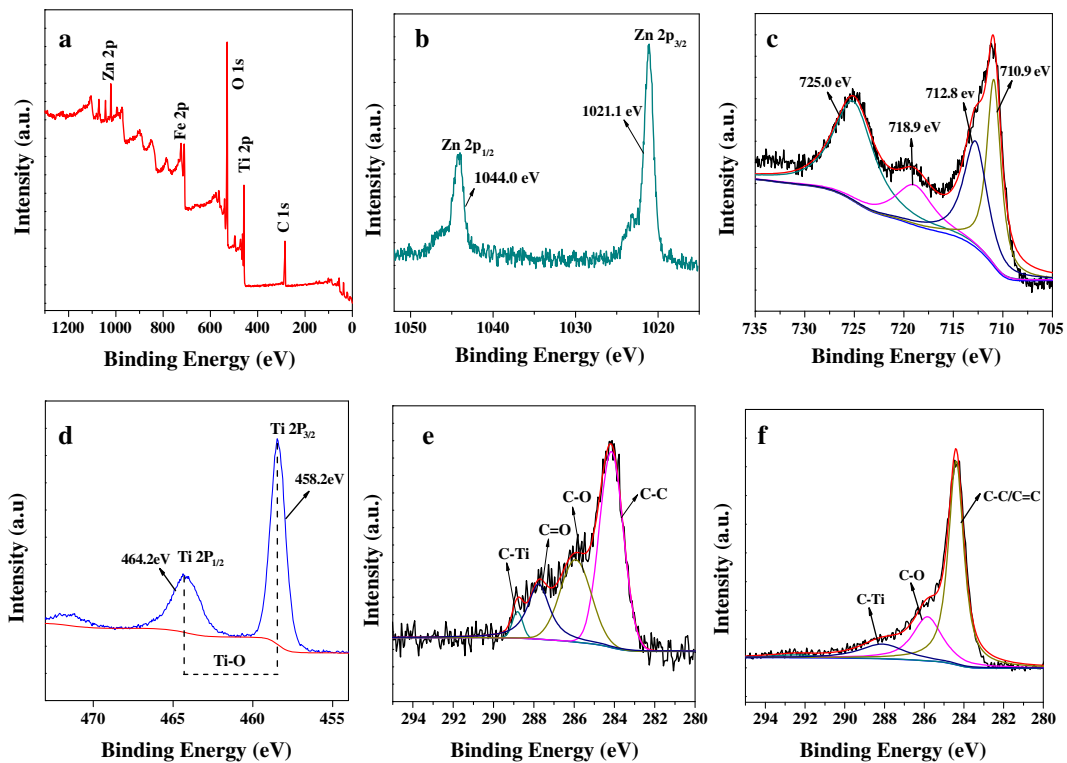


**Fig. 6** XPS spectral of survey scan (a), Zn 2p spectrum (b), Fe 2p spectrum (c), Ti 2p spectrum (d), and deconvolution of C 1s peak before (e) and after (f) thermal reduction of ZF@RGO@TiO<sub>2</sub>

### Magnetic properties

The hysteresis loops of ZF and ZF@RGO@TiO<sub>2</sub> composite were measured by VSM at room temperature. As shown in Fig. 7, the saturation magnetization ( $M_s$ ) value of

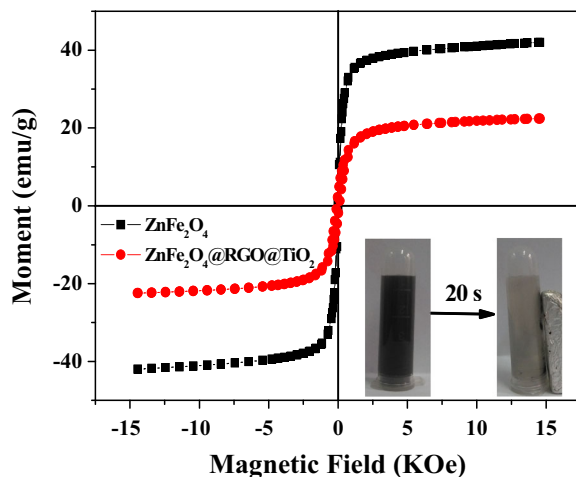


**Fig. 7** Room-temperature magnetization curves of ZF and ZF@RGO@TiO<sub>2</sub> composite. The inset shows that the ZF@RGO@TiO<sub>2</sub> composite suspended in water are attracted to the walls of the vial when a magnet is present for 20 s

ZF is 42.0 emu/g, while the value of ZF@RGO@TiO<sub>2</sub> composite is just 22.4 emu/g, mainly due to the existence of non-magnetic GO and TiO<sub>2</sub> nanoparticles encapsulated on the surface of magnetic ZF particles. However, it cannot be doubtful that the obtained catalysts can be still quickly separated from solution under an external magnetic field, such as seen in the inset picture, which will be beneficial for their reuse and improve practical application in the water purification.

### Evaluation of catalytic efficiency

#### The catalytic activities of different catalysts

To verify the enhanced catalytic activity of the ZF@RGO@TiO<sub>2</sub> composite, several different materials including ZF, P25, ZF@RGO, and ZF@RGO@TiO<sub>2</sub> are chosen to degrade the FA herein, and the results are shown in Fig. 8. It is clear that the degradation efficiency is almost zero with pure H<sub>2</sub>O<sub>2</sub>, suggesting that the degradation is mainly resulted from the catalyst. And, the degradation performance of ZF, P25, and ZF@RGO are not as efficient as the ZF@RGO@TiO<sub>2</sub>.

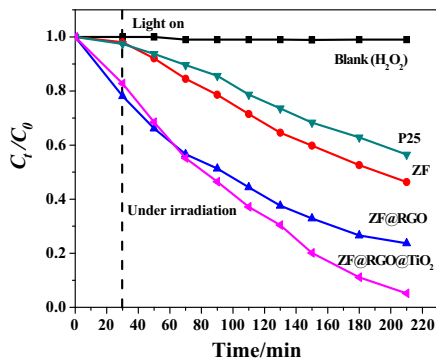


**Fig. 8** Effect of different catalyst on the FA degradation ( $V_{H_2O_2} = 0.8$  mL,  $pH = 7$ )

Especially, both the degradation activity and adsorption ability of the ZF@RGO@TiO<sub>2</sub> composite improve dramatically compared to the ZF and P25. Hence, it can be concluded that the synergic effect of the Fenton oxidation and photocatalytic oxidation do be beneficial to the degradation of FA.

*The influence of catalyst dosage*

The influence of the catalyst dosage on the degradation activity is illustrated in Fig. 9. It can be learned that the degradation activity improves as the amount of the catalyst increases from 0.02 to 0.1 g but drops with excessive dosage. This phenomenon can be ascribed to the reason that the active sites of catalysts increase as the dosage increases from 0.05 to 0.1 g, improving the utilization of visible light and leading to higher degradation rate. When the dosage of catalysts exceeds 0.10 g, the catalyst particles of the as-obtained suspension liquid is too much to hinder the transmission of light and reduce the utilization of light, thus resulting in poor catalytic degradation rate. Additionally, when the

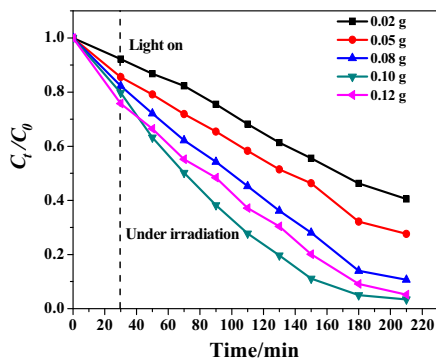


**Fig. 9** Effect of catalyst dosage on FA degradation ( $V_{H_2O_2} = 0.8$  mL,  $pH = 7$ )

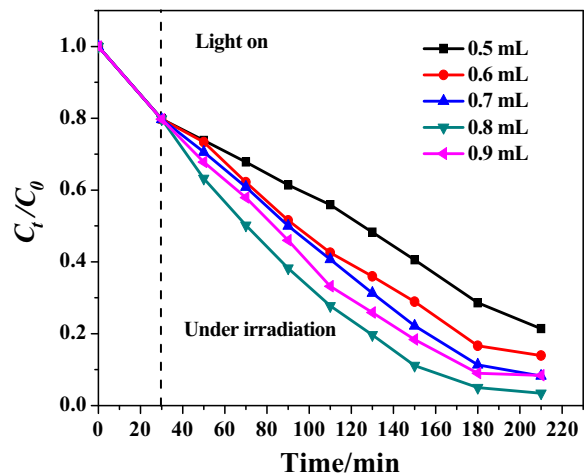


**Fig. 10** Effect of the H<sub>2</sub>O<sub>2</sub> dosage on the FA degradation ( $pH = 7$ )

catalyst is over added, the hydroxyl radicals could be captured by the excess Fe(II) on the surface of the catalyst (Lin et al. 2014).

*The influence of H<sub>2</sub>O<sub>2</sub> dosage*

The effect of H<sub>2</sub>O<sub>2</sub> dosage on FA degradation in this system is investigated and the results are showed in Fig. 10. And, it can be seen that the degradation efficiency of the catalyst on FA solution increases firstly and then decreases with the increasing of H<sub>2</sub>O<sub>2</sub> dosage. As is well known that the H<sub>2</sub>O<sub>2</sub> introduced into the Fenton system can accelerate the generation rate of hydroxyl radicals ( $\cdot OH$ ), which will improve the degradation of the pollutants. Nevertheless, when the amount

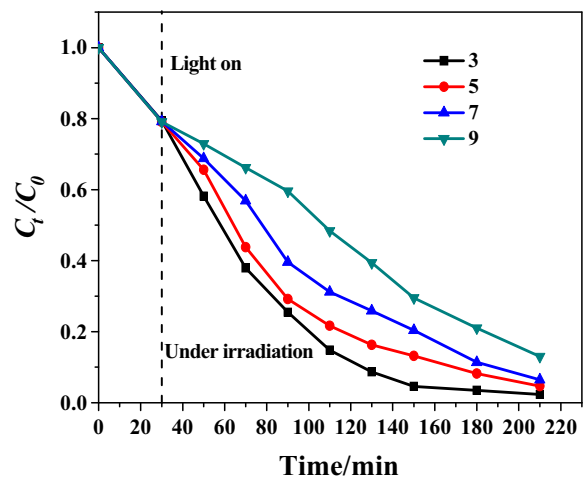


**Fig. 11** Effect of the pH value on the FA degradation ( $V_{H_2O_2} = 0.8$  mL)

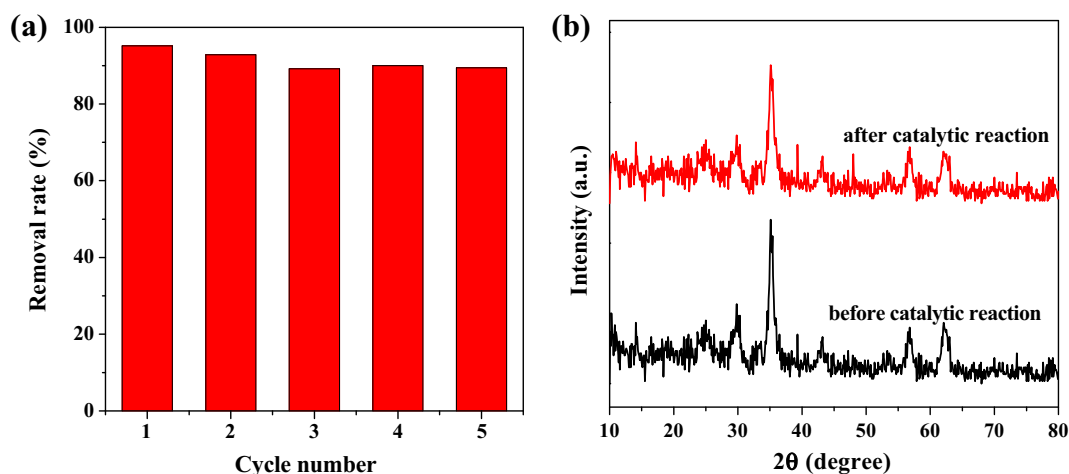


**Fig. 12** The cyclic utilization of the catalyst for degrading FA (a). The XRD patterns of the catalyst before and after 5 cycles (b)

of  $\text{H}_2\text{O}_2$  is achieving a critical point, it can react with the  $\cdot\text{OH}$ , resulting in the degradation efficiency becoming weak (Wang et al. 2015b). Hence, the catalytic performance can only achieve the best when the  $\text{H}_2\text{O}_2$  dosage is the optimal.

#### The influence of pH value

It is known that the pH value has a great influence on the Fenton process. Herein, the degradation activity under different pH is displayed in Fig. 11. And, it can be seen that the catalytic activity is the highest at the pH value of 3 and reaches to 96.4%, while the degradation activity is only 79.8% when the pH value rises to 9. It is reported that Fenton oxidation in general gets the best performance at  $\text{pH} = 2\sim 4$  (Du et al. 2017). And, in this pH range, more hydroxyl radical will be produced to further degrade pollutants. When the pH of the solution increases, the  $\text{OH}^-$  groups will combine with  $\text{Fe}^{3+}$  on the catalyst hydration shell to form the complex  $(\text{Fe}(\text{OH})_6)^-$ . The adsorption of  $\text{H}_2\text{O}_2$  on the catalyst could decrease as the catalyst is covered with  $(\text{Fe}(\text{OH})_6)^-$ , weakening the reaction between catalytic species and  $\text{H}_2\text{O}_2$  (Zhang et al. 2008). Furthermore, the decomposition of  $\text{H}_2\text{O}_2$  into  $\text{H}_2\text{O}$  and  $\text{O}_2$  can be very fast in alkaline solution (Lu et al. 2013), which will not be beneficial to the degradation activity of the catalyst.

#### Stability of ZF@RGO@TiO<sub>2</sub> catalyst

The stability of a catalyst is an important indicator on whether it is promising in the practical application. As

can be seen from Fig. 12a, the activity of the catalyst just slightly decreases with the cycle number increasing. After 5 cycles, it is still up to 90% for degradation of FA. The XRD patterns of the freshly prepared catalyst and the catalyst recycled after 5 cycles are displayed in Fig. 12b. It is found that the crystal structures of the sample do not undergo obvious change, further illustrating that the sample maintains good stability and will possess excellent application prospects in water purification.

#### Catalytic mechanism of ZF@RGO@TiO<sub>2</sub> catalyst

To study the possible catalytic mechanism of the catalysts, the radical trapping experiments are employed in this study. And, silver nitrate ( $\text{AgNO}_3$ ), formic acid ( $\text{HCOOH}$ ), and 2-propanol (IPA) are used to capture the photo-induced electrons ( $e^-$ ), photo-induced holes ( $h^+$ ), and  $\cdot\text{OH}$ , respectively (Yao et al. 2015). As depicted in Fig. 13, in the absence of radical scavengers,

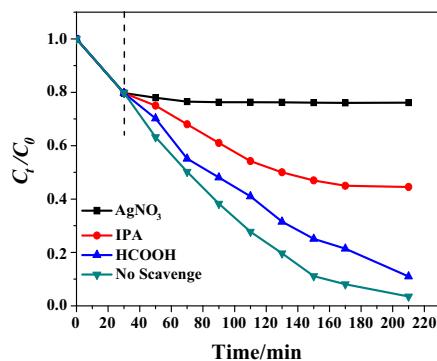


**Fig. 13** The degradation behavior of FA under different scavengers ( $V_{\text{H}_2\text{O}_2} = 0.8$  mL,  $\text{pH} = 7$ )



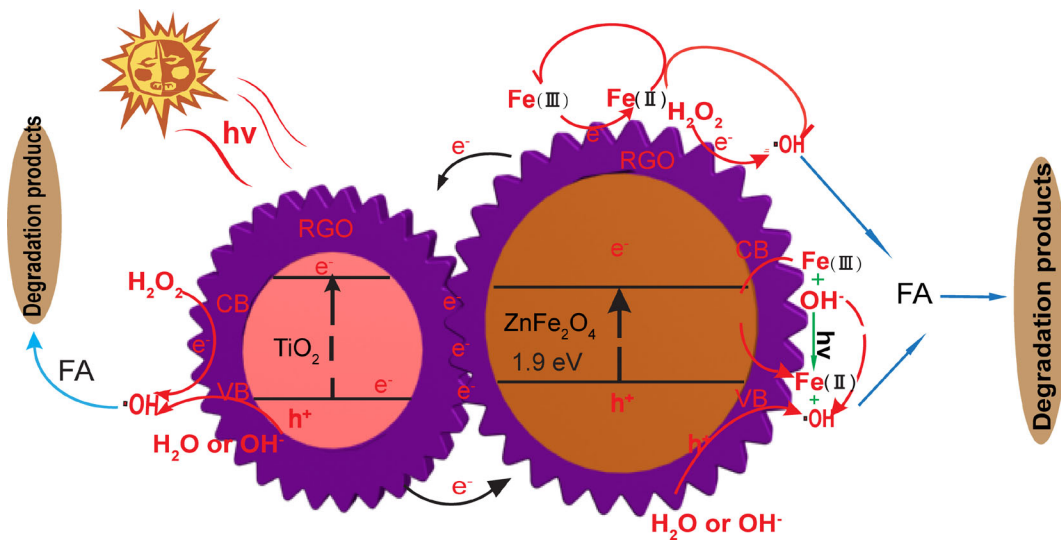


**Fig. 14** Proposed catalytic mechanism of ZF@RGO@TiO<sub>2</sub> composite on FA

the degradation efficiency of FA is up 95.4%. And, on addition of AgNO<sub>3</sub> and IPA, there exhibits a considerable decrease in the degradation efficiency, while the addition of HCOOH does not have a remarkable influence on degrading HA. Hence, it is reasonable to conclude that ·OH, e<sup>-</sup> and h<sup>+</sup> are indeed generated in the catalytic process. Furthermore, the photo-induced e<sup>-</sup> plays the vital role in the catalytic process and it can react with H<sub>2</sub>O<sub>2</sub> or H<sub>2</sub>O in the solution to generate some strong oxidizing species such as ·OH, ·O<sub>2</sub> to degrade directly the pollutants. And, it also can raise the conversion of Fe<sup>3+</sup>/Fe<sup>2+</sup>, improving the catalytic performance of Fenton oxidation. Notably, among of these as-generated strong oxidizing species, ·OH is the main reactive oxidant specie for degrading FA.

As discussed above, the probable catalytic degradation mechanism of ZF@RGO@TiO<sub>2</sub> is shown in Fig. 14. After combined with RGO, the band gap of TiO<sub>2</sub> can be narrowed and will be sensitive to the visible light. Under the visible irradiation, the electrons on VB (valence band) of TiO<sub>2</sub> and ZF can be excited, leading to the generation of e<sup>-</sup> and h<sup>+</sup> on its CB (conduction band) and VB, respectively. The e<sup>-</sup> can be effectively trapped by H<sub>2</sub>O<sub>2</sub> to form ·OH. Simultaneously, Fe(II) can be obtained under visible light irradiation on Fe(III) (Minella et al. 2014). Then, more ·OH can be produced as more Fe(II) is regenerated. Importantly, the photo-induced e<sup>-</sup> can promote the circulation between Fe(III) and Fe(II), so the much more ·OH will be produced. And, the RGO, as the middle layer in the composite, is served as the gear which promotes the photo-induced e<sup>-</sup> flow between the ZF and TiO<sub>2</sub> and

further accelerates the circulation between Fe(III) and Fe(II). Additionally, the rapid transfer of the photo-induced e<sup>-</sup> can prolong the lifetime of the h<sup>+</sup> which can also react with H<sub>2</sub>O or OH<sup>-</sup> to generate the ·OH. Therefore, the degradation of FA is greatly enhanced via visible light irradiation.

## Conclusion

In summary, a multifunctional hierarchical structured ZnFe<sub>2</sub>O<sub>4</sub>@RGO@TiO<sub>2</sub> composite has been successfully synthesized in this work. ZnFe<sub>2</sub>O<sub>4</sub> nanoparticles are encapsulated by RGO which is then coated by anatase TiO<sub>2</sub>. The catalytic activity of the as-prepared ternary catalyst has been explored for degrading FA. And, the results show that the enhanced catalytic activity of the catalyst is due to the synergistic effect of the excellent adsorption of RGO, Fenton oxidation of ZnFe<sub>2</sub>O<sub>4</sub>, and photocatalytic oxidation of TiO<sub>2</sub>. Through exploring the influence of the experimental parameters, it has been found that the H<sub>2</sub>O<sub>2</sub> dosage, solution pH, and catalyst dosage all have a great influence on ZnFe<sub>2</sub>O<sub>4</sub>@RGO@TiO<sub>2</sub> catalytic activity. In addition, the catalyst is reusable and shows 90% efficiency up to 5 cycles. Hence, the developed catalyst will be promising for large-scale degradation of natural organic pollutants under visible light due to its low cost and easy handling.

**Acknowledgments** This author was grateful to the National Nature Science Foundation of China (No 21071125) for financial support for conducting this research work.

## Compliance with ethical standards

**Conflict of interest** The authors declare that they have no conflict of interest.

## References

- An JS, Jho EH, Nam K (2015) Effect of dissolved humic acid on the Pb bioavailability in soil solution and its consequence on ecological risk. *J Hazard Mater* 286:236–241
- Cai C, Zhang ZY, Liu J, Shan N, Zhang H, Dionysiou DD (2016) Visible light-assisted heterogeneous Fenton with  $\text{ZnFe}_2\text{O}_4$  for the degradation of Orange II in water. *Appl Catal B Environ* 182:456–468
- Chen LL, Li L, Wang TT, Zhang LY, Xing SX, Wang CG, Su ZM (2014) A novel strategy to fabricate multifunctional  $\text{Fe}_3\text{O}_4@\text{C}@\text{TiO}_2$  yolk-shell structures as magnetically recyclable photocatalysts. *Nano* 6:6603–6608
- Czech B (2016) The interactions of UV and/or  $\text{H}_2\text{O}_2$  treated CNTOH and CNTCOOH with environmental fulvic acids. *Environ Res* 150:173–181
- Dong YF, Li JH, Li XJ, Zhou BX (2016) The promotion effect of low-molecular hydroxyl compounds on the nanophotocatalytic degradation of fulvic acid and mechanism. *Nano-Micro Lett* 8:320–327
- Du D, Shi W, Wang LZ, Zhang JL (2017) Yolk-shell structured  $\text{Fe}_3\text{O}_4@\text{void}@\text{TiO}_2$  as a photo-Fenton-like catalyst for the extremely efficient elimination of tetracycline. *Appl Catal B Environ* 200:484–492
- Feng JT, Hou YH, Wang XY, Quan WL, Zhang JM, Wang YC, Li LC (2016) In-depth study on adsorption and photocatalytic performance of novel reduced graphene oxide-Zn $\text{Fe}_2\text{O}_4$ -polyaniline composites. *J Alloys Compd* 681:157–166
- Flores N, Sires I, Garrido JA, Centellas F, Rodriguez RM, Cabot PL, Brillas E (2016) Degradation of *trans*-ferulic acid in acidic aqueous medium by anodic oxidation, electro-Fenton and photoelectro-Fenton. *J Hazard Mater* 319:3–12
- Giannakis S, Lopez MIP, Spuhler D, Perez JAS, Ibanez PF, Pulgarin C (2016) Solar disinfection is an augmentable, in situ-generated photo-Fenton reaction—part 1: a review of the mechanisms and the fundamental aspects of the process. *Appl Catal B Environ* 199:199–223
- Hidalgo MC, Murcia JJ, Navo JA, Colon G (2011) Photodeposition of gold on titanium dioxide for photocatalytic phenol oxidation. *Appl Catal A Gen* 39:112–120
- Hou Y, Li XY, Zhao QD, Chen GH (2013)  $\text{ZnFe}_2\text{O}_4$  multi-porous microbricks/graphene hybrid photocatalyst: facile synthesis, improved activity and photocatalytic mechanism. *Appl Catal B Environ* 142:143:80–88
- Hou LR, Lian L, Zhang LH, Pang G, Yuan CZ, Zhang XG (2015) Self-sacrifice template fabrication of hierarchical mesoporous bi-component-active  $\text{ZnO}/\text{ZnFe}_2\text{O}_4$  sub-microcubes as superior anode towards high-performance lithium-ion battery. *Adv Funct Mater* 25:238–246
- Jung HJ, Hong JS, Suh JK (2013) A comparison of fenton oxidation and photocatalyst reaction efficiency for humic acid degradation. *J Ind Eng Chem* 19:1325–1330
- Li J, Sun ZK, Deng YH, Zou Y, Li CY, Guo XH, Xiong LQ, Gao Y, Li FY, Zhao DY (2009) Highly water-dispersible biocompatible magnetite particles with low cytotoxicity stabilized by citrate groups. *Angew Chem* 121:5989–5993
- Li W, Yang JP, Wu ZX, Wang JX, Li B, Feng SS, Deng YH, Zhang F, Zhao DY (2012) A versatile kinetics-controlled coating method to construct uniform porous  $\text{TiO}_2$  shells for multifunctional core-shell structures. *J Am Chem Soc* 134:11864–11867
- Lin H, Zhang H, Wang X, Wang LG, Wu J (2014) Electro-Fenton removal of Orange II in a divided cell: reaction mechanism, degradation pathway and toxicity evolution. *Sep Purif Technol* 122:533–540
- Liu H, Lv T, Zhu ZF (2015a) Template-assisted synthesis of hollow  $\text{TiO}_2@\text{rGO}$  core-shell structural nanospheres with enhanced photocatalytic activity. *J Mol Catal A Chem* 404:405:178–185
- Liu WJ, Cai JY, Ding ZX, Li ZH (2015b)  $\text{TiO}_2/\text{RGO}$  composite aerogels with controllable and continuously tunable surface wettability for varied aqueous photocatalysis. *Appl Catal B Environ* 174-175:421–426
- Liu ZP, Wu WH, Shi P, Guo JS, Cheng J (2016) Characterization of dissolved organic matter in landfill leachate during the combined treatment process of air stripping, Fenton, SBR and coagulation. *Waste Manag* 41:11–118
- Lu DB, Zhang Y, Lin SX, Wang LT, Wang CM (2013) Synthesis of magnetic  $\text{ZnFe}_2\text{O}_4$ /graphene composite and its application in photocatalytic degradation of dyes. *J Alloys Compd* 579:336–342
- Marcano DC, Kosynkin DV, Berlin JM, Sinitskii A, Sun ZZ, Slesarev A, Alemany LB, Lu W, Tour JM (2010) Improved synthesis of graphene oxide. *ACS Nano* 4:4806–4814
- Matilainen A, Vepsäläinen M, Sillanpää M (2010) Natural organic matter removal by coagulation during drinking water treatment: a review. *Adv Colloid Interfaces* 159:189–197
- Minella M, Marchetti G, Laurentiis ED, Malandrino M, Maurino V, Minero C, Vione D, Hanna K (2014) Photo-Fenton oxidation of phenol with magnetite as iron source. *Appl Catal B Environ* 154-155:102–109
- Morais A, Longo C, Araujo JR, Barroso M, Durrant JR, Nogueira AF (2016) Nanocrystalline anatase  $\text{TiO}_2$ /reduced graphene oxide composite films as photoanodes for photoelectrochemical water splitting studies: the role of reduced graphene oxide. *Phys Chem Chem Phys* 18:2608–2616
- Oliveira AG, Nascimento JP, Gorgulho HF, Martelli PB, Furtado CA, Figueiredo JL (2016) Electrochemical synthesis of  $\text{TiO}_2$ /graphene oxide composite films for photocatalytic applications. *J Alloys Compd* 654:514–522
- Oskoei V, Dehghani MH, Nazmara S, Heibati B, Asif M, Tyagi I, Agarwal S, Gupta VK (2016) Removal of humic acid from aqueous solution using UV/ $\text{ZnO}$  nano-photocatalysis and adsorption. *J Mol Liq* 213:374–380
- Rameshbabu R, Ramesh R, Kanagesan G, Karthigeyan A, Ponnusamy S (2014) One pot facile hydrothermal synthesis of superparamagnetic  $\text{ZnFe}_2\text{O}_4$  nanoparticles and their properties. *Sol-Gel Sci Technol* 7:147–151
- Rao GY, Zhang QY, Zhao HL, Chen JT, Li Y (2016) Novel titanium dioxide/iron(III) oxide/graphene oxide photocatalytic membrane for enhanced humic acid removal from water. *Chem Eng J* 302:633–640

- Sehaqui H, Michen B, Marty E, Schaufelberger L, Zimmermann T (2016) Functional cellulose nanofiber filters with enhanced flux for the removal of humic acid by adsorption. *ACS Sustain Chem Eng* 4:4582–4590
- Su L, Feng J, Zhou X, Ren C, Li H, Chen X (2012) Colorimetric detection of urine glucose based ZnFe<sub>2</sub>O<sub>4</sub> magnetic nanoparticles. *Anal Chem* 84:5753–5758
- Trapalis A, Todorova N, Giannakopoulou T, Boukos N, Speliotis T, Dimotikali D, Yu JG (2016) TiO<sub>2</sub>/graphene composite photocatalysts for NO<sub>x</sub> removal: a comparison of surfactant-stabilized graphene and reduced graphene oxide. *Appl Catal B Environ* 180:637–647
- Trellu C, Pechaud Y, Oturan N, Mousset E, Huguenot D, Hullebusch ED, Esposito G, Oturan MA (2016) Comparative study on the removal of humic acids from drinking water by anodic oxidation and electro-Fenton processes: mineralization efficiency and modelling. *Appl Catal B Environ* 194:32–41
- Wang MG, Han J, Xiong HX, Guo R, Yin YD (2015a) Nanostructured hybrid shells of r-GO/AuNP/m-TiO<sub>2</sub> as highly active photocatalysts. *ACS Appl Mater Interfaces* 7:6909–6918
- Wang YB, Zhao HY, Zhao GH (2015b) Iron-copper bimetallic nanoparticles embedded within ordered mesoporous carbon as effective and stable heterogeneous Fenton catalyst for the degradation of organic contaminants. *Appl Catal B Environ* 164:396–406
- Wang TC, Qu GZ, Ren JY, Yan QH, Sun QS, Liang DL, Hu SB (2016) Evaluation of the potentials of humic acid removal in water by gas phase surface discharge plasma. *Water Res* 89: 28–38
- Wu ZB, Dong F, Zhao WR, Wang HQ, Liu Y, Guan BH (2009) The fabrication and characterization of novel carbon doped TiO<sub>2</sub> nanotubes, nanowires and nanorods with high visible light photocatalytic activity. *Nanotechnology* 20:235701
- Wu SK, Shen XP, Zhu GX, Zhou H, Ji ZY, Chen KM, Yuan AH (2016) Synthesis of ternary Ag/ZnO/ZnFe<sub>2</sub>O<sub>4</sub> porous and hollow nanostructures with enhanced photocatalytic activity. *Appl Catal B Environ* 184:328–336
- Yan WY, Zhou Q, Chen X, Yang Y, Zhang Y, Huang XJ, Wu YC (2016) Size-controlled TiO<sub>2</sub> nanocrystals with exposed {001} and {101} facets strongly linking to graphene oxide via p-Phenylenediamine for efficient photocatalytic degradation of fulvic acids. *J Hazard Mater* 314:41–50
- Yang D, Feng J, Jiang LL, Wu XL, Sheng LZ, Jiang YT, Wei T, Fan ZJ (2015) Photocatalyst interface engineering: spatially confined growth of ZnFe<sub>2</sub>O<sub>4</sub> within graphene networks as excellent visible-light-driven photocatalysts. *Adv Funct Mater* 25:7080–7087
- Yao Y, Lu F, Zhu Y, Wei F, Liu X, Lian C, Wang S (2015) Magnetic core-shell CuFe<sub>2</sub>O<sub>4</sub>@C<sub>3</sub>N<sub>4</sub> hybrids for visible light photocatalysis of Orange II. *J Hazard Mater* 297:224–223
- Zhang JB, Zhuang J, Gao LZ, Zhang Y, Gu N, Feng J, Yang DL, Zhu JD, Yan XY (2008) Decomposing phenol by the hidden talent of ferromagnetic nanoparticles. *Chemosphere* 73: 1524–1528
- Zhou X, Li XW, Sun HB, Sun P, Liang XH, Liu FM, Hu XL, Lu GY (2015) Nanosheet-assembled ZnFe<sub>2</sub>O<sub>4</sub> hollow microspheres for high sensitive acetone sensor. *ACS Appl Mater Interface* 7:15414–15421